communications
physics

ARTICLE

https://doi.org/10.1038/s42005-022-00961-9 OPEN

Ultrafast interfacial carrier dynamics and persistent topological surface states of Bi_2Se_3 in heterojunctions with VSe_2

Tae Gwan Park[1], Jae Ho Jeon[2], Seung-Hyun Chun[2], Sunghun Lee[2]✉ & Fabian Rotermund[1]✉

Vanadium diselenide (VSe_2) has recently been highlighted as an efficient 2D electrode owing to its extra-high conductivity, thickness controllability, and van der Waals contact. However, as the electrode, applications of VSe_2 to various materials are still lacking. Here, by employing ultrafast time-resolved spectroscopy, we study VSe_2-thickness-dependent interfacial effects in heterostructures with topological insulator Bi_2Se_3 that is severely affected by contact with conventional 3D electrodes. Our results show unaltered Dirac surface state of Bi_2Se_3 against forming junctions with VSe_2, efficient ultrafast hot electron transfer from VSe_2 to Bi_2Se_3 across the interface, shortened metastable carrier lifetimes in Bi_2Se_3 due to dipole interactions enabling efficient current flow, and the electronic level shift (~tens meV) of bulk states of Bi_2Se_3 by interfacial interactions, which is ~10 times lower compared to conventional electrodes, implying weak Fermi level pinning. Our observations confirm VSe_2 as an ideal electrode for efficient Bi_2Se_3-based-applications with full utilization of topological insulator characteristics.

---

[1] Department of Physics, Korea Advanced Institute of Science and Technology (KAIST), Daejeon 34141, Republic of Korea. [2] Department of Physics and Astronomy, Sejong University, Seoul 05006, Korea. ✉email: kshlee@sejong.ac.kr; rotermund@kaist.ac.kr

Topological insulators (TIs) are a class of electronic materials that possess ordinary insulating states in the bulk and topologically protected metallic states at the surface[1,2]. The topological surface state with massless Dirac fermions exhibits unique properties of spin-momentum locking ensured by Z_2 invariant in three-dimensional (3D) TIs including Bi_2Se_3. A spin-polarized and defect-tolerant conducting channel of these TIs enables promising electronic, optoelectronic, and spintronic applications[2,3], such as ultralow-power tunnel transistor[4,5], opto-spintronics with polarized photocurrent[6,7], high-performance broadband photodetector[8,9], and nonvolatile memory by spin-transfer torque[10]. For device applications in transistors or external circuits, contact with metal electrodes plays a crucial role. However, in the junction with metal electrodes for producing transistors or external circuits, unexpected contact issues occur for several reasons such as interfacial hybridization and defects during the manufacturing process, leading to relaxation of spin-momentum locking and large contact resistance by strong Fermi level pinning (FLP)[11,12]. This can severely degrade the device performance. Moreover, an inherent low dimensionality and the existence of Dirac surface state (DSS) make the material systems themselves very sensitive to the junction interfaces. Although several conventional 3D metals[13–16], including Au, Cr, Ti, and Pd, have been adopted in Bi_2Se_3-based applications, the interfacial study of Bi_2Se_3-based junction has shown that there exist still several contact issues to be solved except for Au, which exhibits weak interfacial interaction with Bi_2Se_3[12].

A similar issue for the metal electrode contact has appeared at 2D semiconducting transition metal dichalcogenides (s-TMDs)[17–19], which are critically affected by such interactions with metal electrodes owing to their inherent atomically thin thickness and low dimensionality. As a breakthrough strategy, van der Waals (vdW) contact has been illuminated to form atomically sharp interfaces and suppress chemical interactions at interfaces between two dissimilar materials[18–22]. The vdW metal-semiconductor junctions (MSJs) have been recently demonstrated as the ideal junction interfaces by transferring graphene[21,23–25] or noble 3D metal films[18–20]. The desire for realizing an ideal junction interface and optimized metal electrode materials leads to considerable interest in metallic TMDs (m-TMDs) beyond graphene[21,26–29]. The m-TMDs have been successfully adopted as metal electrodes for s-TMD because they provide weak FLP in vdW MSJs[21], high field-effect mobility in VTe_2/MoS_2[28], low contact resistance in VS_2/MoS_2[29] with high functionality, an integrated external circuit with advantages of high-conductivity, tunable thickness, and van der Waals epitaxial contacts[26], in contrast to the use of conventional 3D metals. Among m-TMDs, VSe_2, which exhibits thickness controllability and extra-high (10^2–10^4 order) electrical conductivity compared to other 2D materials, turned out to be a promising electrode material[27]. Recently, VSe_2 at metallic 1T-phase has been applied as the electrode in diverse 2D material systems such as VSe_2/WSe_2, $VSe_2/MoSe_2$ vdW MSJs with low contact resistance[30], efficient electrocatalysts for Li-S batteries[31], and superior K-ion storage[32]. Thus, it is considered important to expand and elucidate the role of VSe_2 as the metal electrode in diverse material systems where the contact issue still remains.

In this work, we investigate the interfacial junction in VSe_2/Bi_2Se_3 heterostructures (VBHs) by employing ultrafast optical spectroscopy in reflection geometry. This allows us to examine

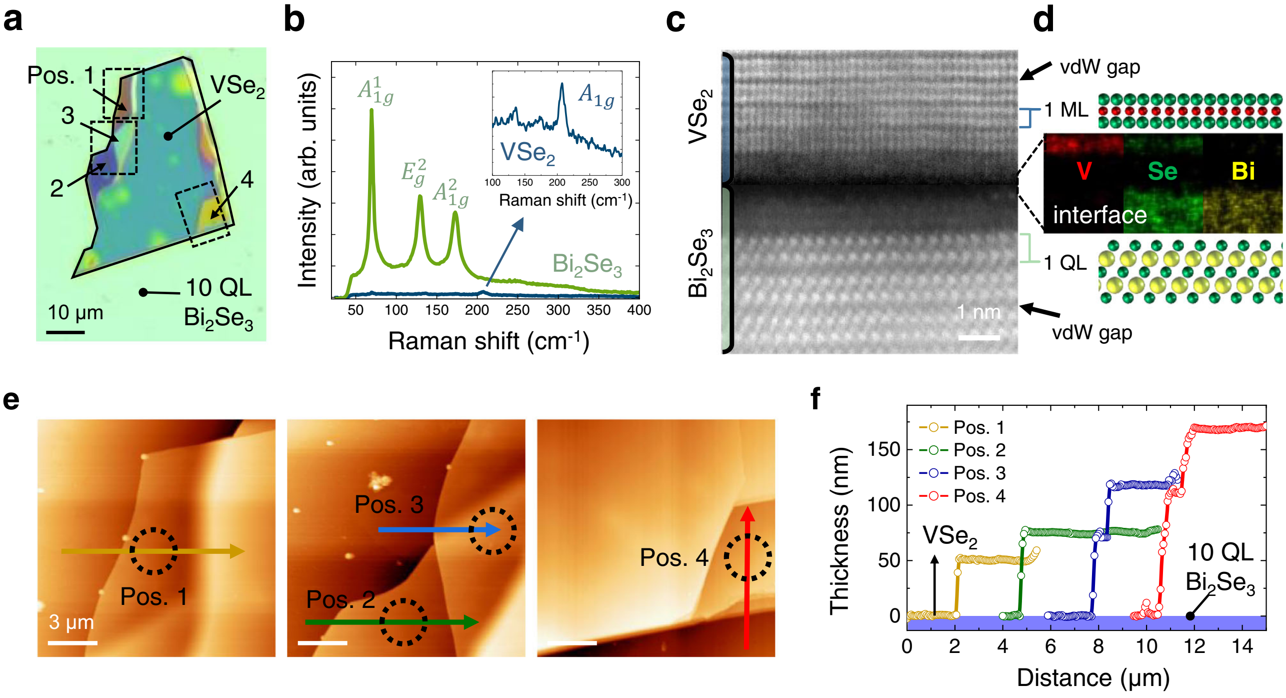

Fig. 1 Structural information and morphology of VSe2/Bi2Se3 heterostructures (VBHs). **a** Optical image of VBHs. The regions of interest are marked as positions 1-4. The black solid line marks the boundaries of the VSe_2 flake and the black dashed line indicates the VSe_2 region of interest for this study. **b** Raman spectra of VSe_2 and Bi_2Se_3. Inset, enlarged Raman spectra of VSe_2. Each Raman active mode is indicated. **c** Cross-sectional high-angle annular dark-field scanning transmission electron microscopy (HAADF-STEM) image of a VBH. The interface between VSe_2 and Bi_2Se_3 shows the empty space of the carbon protective layer deposited before slice cutting by a focused ion beam. The clear vdW gap and atomic configuration are shown. **d** Corresponding energy-dispersive X-ray spectroscopy (EDS) elemental intensity maps for V, Se, and Bi along with a related schematic of the atomic structure. Note that the data of cross-sectional HAADF-STEM and EDS, which are required for deposition of carbon protecting layer, were collected after completing pump-probe experiments. **e** Atomic force microscopy (AFM) topography images of VBHs at positions 1–4. The dashed circles indicate the spots of interest in the pump-probe measurements. The scale bar is the same for all three images. **f** Height profiles along with the arrows at positions 1–4. Note that the measured height is the thickness of VSe_2 on Bi_2Se_3.

the interfacial phononic/carrier dynamics in a highly sensitive manner[33–35]. Since the photoexcited carriers in Bi_2Se_3 are quite sensitive to the topological state[36–38] and Fermi level[39,40], crucial information on certain modulation of both DSS and bulk state of Bi_2Se_3 by junctions with metallic VSe_2 can be obtained. An electron microscope and interfacial acoustic phonon dynamics show a good quality of interfacial contact in the VBHs. The hot electron transfer from VSe_2 to Bi_2Se_3 across the interfaces in ultrashort timescale (~100 fs) leads to the improved efficiency of Bi_2Se_3-based optoelectronic devices. In addition, the photoexcited carrier dynamics in VBH provide direct evidence of unaltered DSS of Bi_2Se_3 by the contact with VSe_2. The VSe_2-thickness-dependent spectral and dynamical response in the VBHs quantitatively gives electronic modulation of the bulk band in Bi_2Se_3, which originated by interfacial dipole interactions due to the charge transfer/redistribution for thermal equilibrium. The observed electronic level shifts of Bi_2Se_3 by the junction with VSe_2 are ~10 times lower compared to the junction with conventional 3D metals, indicating weak FLP. The lifetime of metastable carriers in Bi_2Se_3 is shortened by 3 times due to dipole interactions in VBH, enabling highly efficient current flow. Overall results suggest that VSe_2 can be considered as a promising candidate for the vdW metal electrode in Bi_2Se_3-based diverse applications by fully utilizing the superior characteristics of topological insulators.

Results and discussion

Preparation and characterization of VBHs. For the investigation, single-crystalline metallic 1T-VSe_2 was grown by a chemical vapor transport method and transferred onto a 10 quintuple layer (QL) Bi_2Se_3 thin film by mechanical exfoliation. The carrier concentration (N_0) of Bi_2Se_3 was approximately $N_0 = 3.13 \times 10^{20}\,\mathrm{cm^{-3}}$ based on the Hall resistivity measurements (see Supplementary Fig. 1). The hall resistance of 10 QL Bi_2Se_3 shows the characteristics of an n-type Bi_2Se_3. As marked positions by black arrows in Fig. 1a, we were able to achieve different thicknesses of VSe_2 on Bi_2Se_3 in a single flake. The size of a VSe_2 flake on Bi_2Se_3 was sufficiently large compared to the spatial resolution (<2 μm) of our spectroscopic system, and imperfectly exfoliated VSe_2 flakes showed regions with different thicknesses, enabling us to investigate the VSe_2-thickness-dependent phononic and carrier dynamics of Bi_2Se_3. Different positions of VSe_2 with different thicknesses were marked as Pos. 1 to 4, as shown in Fig. 1a (additionally see Fig. 1e, f). The conspicuous and clear Raman modes (Fig. 1b) and high-angle annular dark-field scanning transmission electron microscopy (HAADF-STEM) image (Fig. 1c) confirmed that both VSe_2 and Bi_2Se_3 had a high-quality single-crystalline nature. Note that Fig. 1b shows the Raman spectra measured in individual VSe_2 and Bi_2Se_3, since only the predominant VSe_2 Raman peak at 206 $\mathrm{cm^{-1}}$ was obtained from the VBH owing to relatively thick VSe_2, which obscures the weak Raman signal of Bi_2Se_3 at appropriate laser powers below the VSe_2 damage threshold. Each Raman mode showed in good agreement with the previous studies of 1T-VSe_2 and Bi_2Se_3[41,42]. Note that the absence of Raman mode of the semiconducting 2H-VSe_2 at 190 $\mathrm{cm^{-1}}$,[43] which can be formed by structural phase transition during the preparation process, implies that the VSe_2 used in this study was a pure metallic 1T-phase. The thicknesses of VSe_2 at the marked positions (1, 2, 3, and 4) were measured to be 48, 74, 118, and 167 nm on 10 QL Bi_2Se_3 by atomic force microscopy (AFM), respectively (Fig. 1f). The root means square roughness extracted from the AFM images (Fig. 1e) was quite low (under ~0.1 nm), indicating a clean and smooth surface.

Interfacial coherent acoustic phonon (CAP) dynamics in VBHs. To verify superior interfacial contact between VSe_2 and Bi_2Se_3 in a large area, collinearly aligned two-color pump–probe spectroscopy was carried out on VBHs. The pump (1.5 eV) and probe (~0.93–0.95) pulses were normally incidents on the VBHs with a time delay. The pump fluence was ~12 μJ/cm^2 and the probe fluence was kept sufficiently weak about two orders of magnitude compared to the pump beam. Time-resolved reflectance measurements were performed at each position of the VBHs. The inset of Fig. 2a illustrates a schematic of the process, where coherent acoustic phonons (CAPs) occurred at the interfaces of VBHs. The acoustic wave was generated at the VBH interfaces by the incident optical pulse and propagated into the VSe_2 flake. Figure 2a shows the background-free CAPs in 10 QL Bi_2Se_3 and 118 nm VSe_2/10 QL Bi_2Se_3 (118 nm VBH) obtained by abstraction from the fitting with a biexponential representing the decay dynamics (more details in Supplementary Note 1). Earlier CAP before 40 ps and later echo signals around 80 ps time delay were observed. For the earlier CAP part, the oscillation frequencies of CAPs were obtained by fitting with damped oscillation functions as 125 and 43 GHz. The obtained frequencies well matched the interlayer vibrational modes in 10 QL Bi_2Se_3, in which the frequency depended on the number of layers[42,44]. Note that the CAP signal of Bi_2Se_3 was observed in both Bi_2Se_3 and the VBH at the same time delay. This result reflected that Bi_2Se_3 was almost directly excited by the optical pulse.

After damping of the inherent earlier CAP signal in Bi_2Se_3, subsequent echo signals were observed. The acoustic wave generated by the optical pump reciprocated in VSe_2 by reflection at the air and Bi_2Se_3 interface as shown in the inset of Fig. 2a. When the acoustic wave arrived at the VSe_2-Bi_2Se_3 interface, echo signals appeared with different intervals depending on the thickness of VSe_2 (Fig. 2b). The acoustic waves at interfaces can be described by the acoustic mismatch (AM) model for boundary conditions of continuous displacement and stress. This indicates perfect and atomically flat interfaces in our case[45]. Based on AM model, the amplitude reflection coefficient is given by

$$r_{ij} = (Z_j - Z_i)/(Z_j + Z_i) \qquad (1)$$

Here, $Z = \rho v_s$ is the acoustic impedance of material, where ρ and v_s are the density and the sound speed, respectively. The amplitude reflection coefficients of interfacial CAP were estimated to be $r_{VSe_2-air} \approx -1$ and $r_{VSe_2-Bi_2Se_3} = 0.29$ with $Z_{Bi_2Se_3} = 21.78$[46], $Z_{VSe_2} = 12$, and $Z_{air} = 0.0004$ with a unit of $10^6\,\mathrm{kg\,m^{-2}\,s^{-1}}$. The negative reflection coefficient indicates that the phase of the reflected acoustic wave is changed by π. Hence, the reflected echo exhibits a phase shift of π with each round trip, resulting from the reflection at the air interfaces. In the case of the heterostructure of 118 nm VSe_2 and 10 QL Bi_2Se_3 (118 nm VBH in Fig. 2a), the first echo was observed at 87 ps, and subsequently, the second and third echoes emerged with alternating phases at the same interval of 86 ps. The similar times of the first echo (87 ps) and the interval (86 ps) imply that acoustic waves were launched from Bi_2Se_3 through hot phonons and interlayer vibration after photoexcitation. Note that the reflected acoustic waves at the interface of Bi_2Se_3/Al_2O_3 substrate were negligible in our analysis because the reflection coefficient of Bi_2Se_3/Al_2O_3 is 0.18 with the acoustic impedance for $Z_{Al_2O_3} = 31.5 \times 10^6\,\mathrm{kg\,m^{-2}\,s^{-1}}$ [47] does not change the phase of acoustic waves. Moreover, the expected echo interval in Bi_2Se_3 at 3.4 ps, where the thickness of Bi_2Se_3 is 10 nm and the sound speed is 2.9 $\mathrm{km\,s^{-1}}$, is substantially short compared to that observed in VSe_2. The phase was also not changed by reflection at Bi_2Se_3/Al_2O_3 interfaces, thus, we safely concluded that the echo signals were observed when the acoustic waves reached the interface at VSe_2/Bi_2Se_3.

The observed time intervals between echoes of 42, 54, 86, and 111 ps in the 48, 74, 118, and 167 nm VBHs, respectively (Fig. 2b),

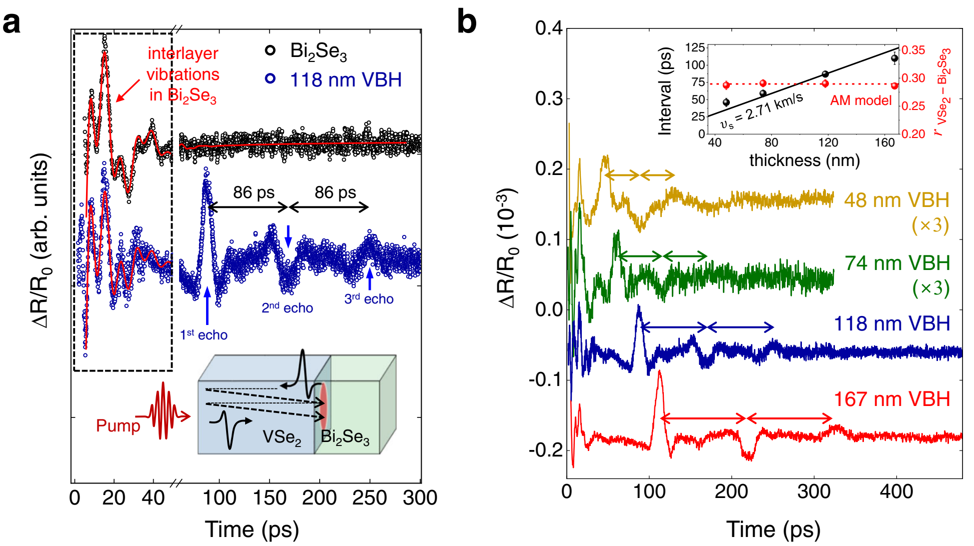

Fig. 2 Thickness-dependent coherent acoustic phonon (CAP) dynamics of VSe2/Bi2Se3 heterostructures (VBHs). **a** Pump-probe signals of VSe_2-thickness-dependent background-free CAPs of VBHs with ~0.93 to 0.95 eV probe energy, where $\Delta R/R_0$ represents the transient reflectance. The dashed box indicates the CAP signals from 10 quintuple layer (QL) Bi_2Se_3. The upward/downward arrows indicate acoustic pulse echoes at the VSe_2/Bi_2Se_3 interfaces. Simplified schematic of pump–probe experiments and Dynamic illustration of acoustic waves in VSe_2 generated by optical pump pulses and reciprocated by reflection at the air and Bi_2Se_3 interfaces (Inset). The red curves indicate fitting results with damped oscillation of interlayer vibrations in Bi_2Se_3. The time intervals between echoes (~86 ps) are listed. **b** VSe_2-thickness dependent interfacial CAP dynamics of VBHs. Obtained echo interval (black dots) versus VSe_2 thickness and amplitude reflection coefficient (red dots) (Inset). The line fit (black line) to the interval data provides the sound speed of VSe_2 (2.71 km s^{-1}). Inset: The dash red line indicates the predicted reflection coefficient based on the acoustic mismatch model for the atomically flat interface.

exhibited a linear dependence on the VSe_2 thickness, which means that so did the transit round-trip time of the acoustic wave in VSe_2. The inset of Fig. 2b shows the VSe_2-thickness-dependent time interval between echoes at each VBH, with a sound velocity of VSe_2 of $v_s = 2.71$ km s^{-1} estimated from the linear dependence. This value is close to the previously reported value of 2.67 km s^{-1} [48]. In general, defects and imperfect contact can reduce the coherence of acoustic waves and induce different frequencies, which are independent of the material thickness[45]. Moreover, as shown in the inset of Fig. 2b, the different amplitudes between echoes were consistent with the reflection coefficient of $r_{VSe_2-Bi_2Se_3} = 0.29$, while r_{VSe_2-air} was near unity, providing direct evidence of an atomically flat interface with negligible defects or poor contact of the VBHs[49]. Consequently, the interface of each VBH was assumed to be nearly perfect, and the effects of additional gap states due to defects that hinder the interpretation of the results could be excluded.

Ultrafast hot electron dynamics of Dirac surface states at VBHs. With the VBHs possessing a high-quality interface, we performed transient reflectance (TR) measurements to investigate the interfacial carrier dynamics in the DSS and the bulk electronic states of Bi_2Se_3 in VBHs. In TR measurements with a pump fluence of 12 μJ cm^{-2}, the photoexcited carrier density estimated from the power density along with the complex refractive index of Bi_2Se_3[50] was 1.6×10^{19} cm^{-3}, which is only 5% of the background carrier concentration and implies a small perturbation to the charge carriers in Bi_2Se_3. Figure 3a shows TR spectra for 10 QL Bi_2Se_3, bare VSe_2, and 118 nm VBH. For bare Bi_2Se_3, the TR spectral responses were significantly different before and after ~2 ps. Just after photoexcitation, the negative differential reflectance ($\Delta R/R_0$) at overall probe energies was observed before 2 ps, whereas, after 2 ps, a derivative-like TR response, *i.e.* changing the TR sign from negative to positive according to probe energy, was observed. Since the observed carrier dynamics are complex due to the coexistence of the metallic surface state and insulating bulk state of Bi_2Se_3 thin film in optical spectroscopy[37,51], a clear distinction is necessary for each contribution. The overall negative $\Delta R/R_0$ before 2 ps was confirmed by the transient absorption (TA) measurement results (see Supplementary Note 2) to be related to the photobleaching through the injection of hot carriers[51,52] as indicated by stage (i) in Fig. 3b. After hot carrier injection, the rapid decay with 2.5 ps, as indicated τ_1 and stage (ii), was attributed to the intraband relaxation by electron-LO (longitudinal-optical) phonon scattering of excited carriers in bulk and surface states of Bi_2Se_3[37,51,52], which implies a dominant contribution of the DSSs on carrier dynamics in Bi_2Se_3 thin film. After surface scattering relaxation, the derivative-like TR spectra (positive $\Delta R/R_0$ to negative $\Delta R/R_0$ according to probe energy) with a long lifetime appeared after ~5 ps. The derivative TR with a long decay time was similar to the previously reported relaxation time of the bulk state toward their respective bottom bands, *i.e.* conduction band minimum/valence band maximum (CBM/VBM) for the bulk state[51]. The derivative-like TR spectra and their decay dynamics, which are commonly observed in semiconductors by excitonic effects or state filling by photoexcitation[33–35], can be regarded as a signature of the insulating bulk band of Bi_2Se_3 as discussed in the following section.

For bare VSe_2 on SiO_2 substrate with a thickness of about 100 nm (see Supplementary Fig. 4a in Supplementary Note 3), the TR spectra show a negative $\Delta R/R_0$ in overall delay time and probe energy. The probe energy used in our experiments was on the order of 1 eV, which corresponds to the photobleaching of intraband transition because the estimated energy difference between the Fermi energy and valence band maximum was about 1.7 eV reported in the previous theoretical calculations for the non-magnetic 1T-VSe_2[53,54]. The excited electron dynamics of VSe_2 were considerably slow compared to Bi_2Se_3 as shown in Fig. 3b. The excited electrons in VSe_2 did not recover at all within a given time window (only 10–25% even within 300 ps time delay,

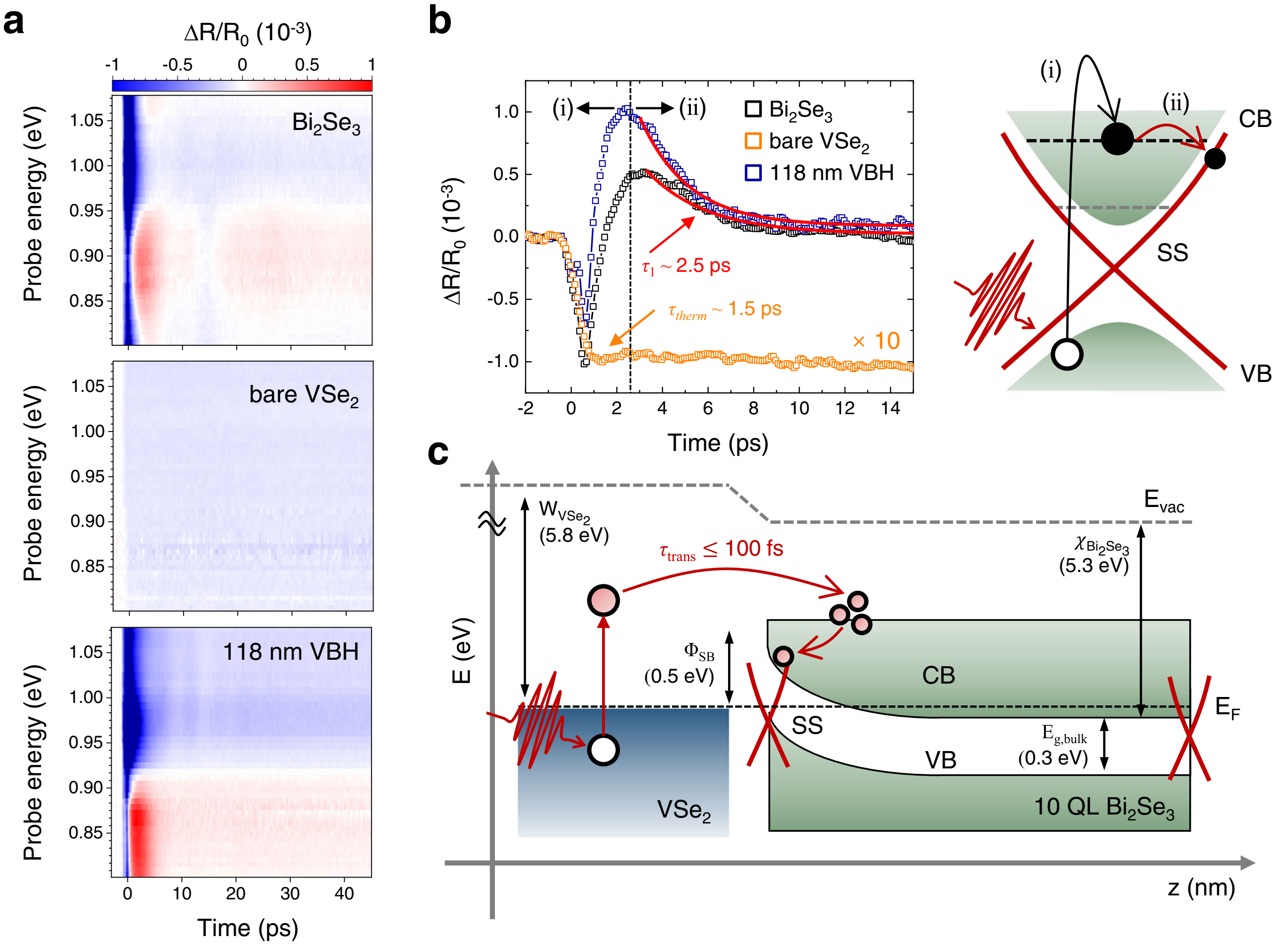

Fig. 3 Ultrafast interfacial hot electron transfer and relaxation dynamics in VSe2/Bi2Se3. a 2D plots of the transient reflectance (TR) spectra of 10 quintuple layer (QL) Bi_2Se_3, bare VSe_2 film, and 118 nm VSe_2/Bi_2Se_3 Heterostructure (VBH). **b** TR traces at each sample around 0.9 eV probe energy. The thermalization time (τ_{therm}) of bare VSe_2 and decay time of phonon-assisted bulk-surface scattering (τ_1, red curves) are listed. The stages of (i) and (ii) indicate the processes of ultrafast carrier dynamics in Bi_2Se_3. The CB, VB, and SS means conduction band, valence band, and surface state, respectively. **c** Schematic of band alignment and hot electron transfer dynamics in VBHs and. Each characteristic energy of the work function (W) of VSe_2, electron affinity (χ), and bandgap (E_g) of Bi_2Se_3 is shown according to previous studies[11,14,62].

as shown in Supplementary Fig. 4b). This slow recovery characteristic can be influenced by very flat V-3d orbitals with energy of ~1 eV where the excited electrons mainly located. Subsequently, the e-ph scattering rate is expected to be extremely low compared to Au[55] and graphene[56] in terms of energy/momentum conservation. It seems to be a decay on the order of ns as shown in Supplementary Fig. 4b. Such a slow decay can be attributed to lattice contribution[57]. A similar level of decay property was found in the lattice temperature recovery time for Au thin film[58]. The TR traces in VSe_2 showed a fast-negative rise within ~1.5 ps and subsequent slow decay. Although the thermalization time (τ_{therm}) of hot electrons in VSe_2 is about 1.5 ps, similar to the monolayer case[59], the TR response is quite distinguishable, indicating that the excited electron dynamics have a thickness dependence as for other TMD systems[60,61]. Interestingly, for 118 nm VBH, the TR response and kinetics are almost the same as Bi_2Se_3. Furthermore, it is noteworthy that the positive $\Delta R/R_0$ at VBH is improved by ~2 times compared to Bi_2Se_3 thin film, although the $\Delta R/R_0$ for bare VSe_2 flakes is negative. The expected hot electron transfer time (τ_{trans}) from VSe_2 to Bi_2Se_3 is comparable or faster than 100 fs. About 10 times faster electron transfer compared to the relaxation time of hot electrons in VSe_2 indicates that the photoexcited electrons in VSe_2 are directly transferring into Bi_2Se_3 before thermalization owing to the fast decay channel of Bi_2Se_3 (Fig. 3c). This is consistent with the previously reported VSe_2/graphene heterostructures[59]. Fig. 3c shows the band diagram after junction in VBH. The work function (W) of VSe_2 is 5.8 eV[62] and the electron affinity (χ) of Bi_2Se_3 is 5.3 eV[11] with the bulk bandgap ($E_{g,\ bulk}$) of 0.3 eV[14], which creates an upward band bending of Bi_2Se_3[63] and n-type junction with Schottky barrier height (SBH, ΦSB) of about 0.5 eV. Accordingly, the photoexcited electrons in VSe_2 with a 1.5-eV optical pump can transfer energetically into Bi_2Se_3, which has a fast decay channel through the DSS, across the vdW gap. The observed larger magnitude $\Delta R/R_0$ and similar time constant of τ_1 in VBH imply that the excited electrons in VSe_2 can transfer to the bulk band in Bi_2Se_3 within an ultrashort timescale (~100 fs), then efficiently relaxed by scattering with the DSS of Bi_2Se_3 as illustrated in Fig. 3c.

Ultrafast carrier dynamics of insulating bulk states at VBHs. After the intraband relaxation process, a relatively long lifetime of carriers in the bulk band induced the derivative-like TR response, representing the optical transition in the insulating bulk band of Bi_2Se_3 that was maintained for several hundred ps. The increased reflectance (red color) at lower energy and decreased reflectance (blue color) at higher energy were observed at the boundary of ~0.96 eV in Bi_2Se_3 and VBH (Figs. 3a, 4a). The shape of TR

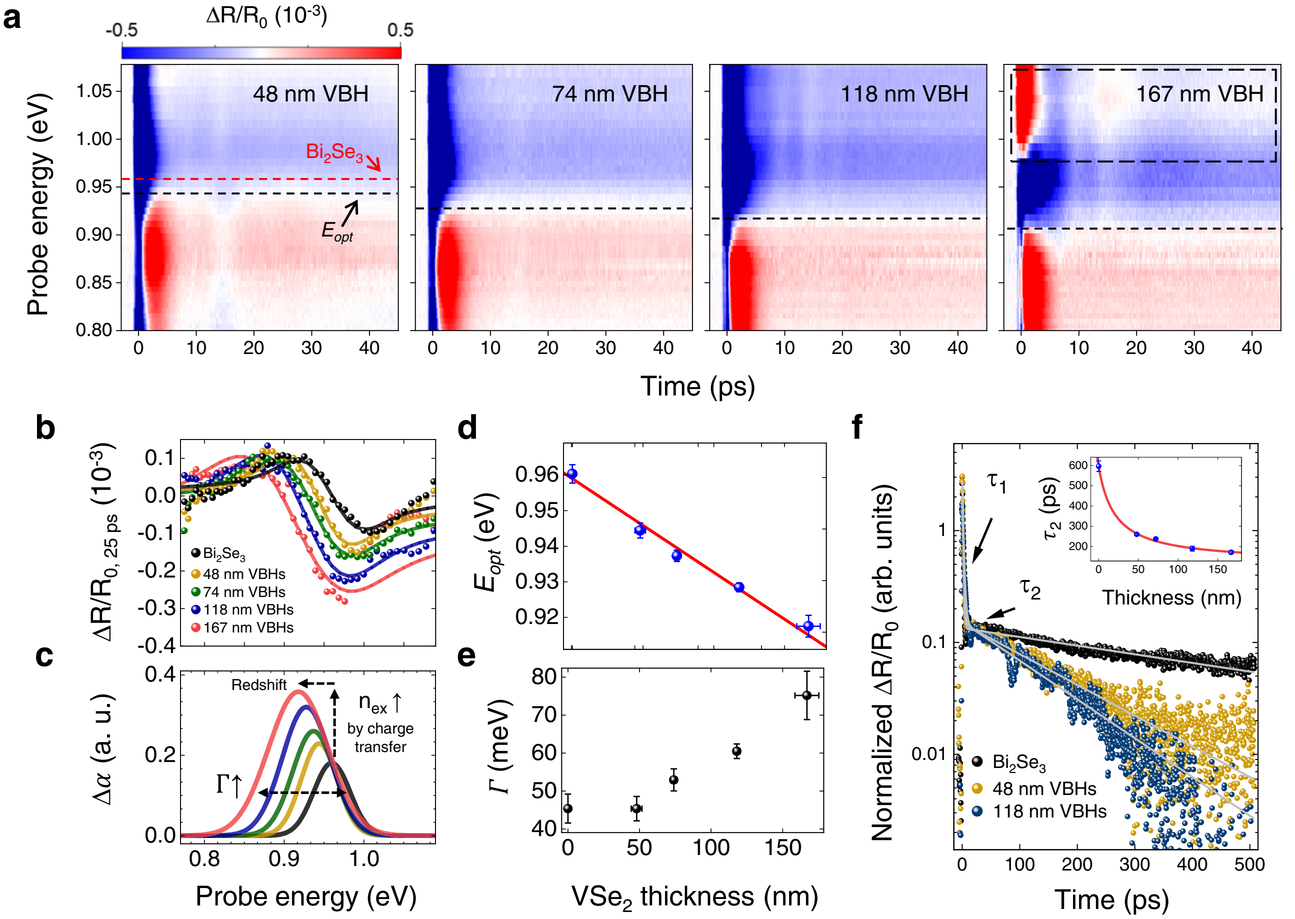

Fig. 4 VSe2-thickness-dependent electronic modulation of insulating bulk states in Bi2Se3. **a** 2D plots of the transient reflectance (TR) spectra of VSe_2/Bi_2Se_3 heterostructures (VBHs). The dashed horizontal lines indicate the optical transition energy (E_{opt}) of 10 quintuple layer (QL) Bi_2Se_3 (red) and VBHs (black), respectively. **b** Selected TR spectral features at 25 ps with fitting curves based on Eq. (4) and (**c**) corresponding absorption changes ($\Delta\alpha$). The n_{ex} and Γ represent the photoexcited carrier concentration and broadening factor of photoinduced absorption changes, respectively. **d** VSe_2-thickness-dependent E_{opt} obtained by fitting from (b). The line fit delivers a slope of 0.26 meV nm^{-1}. **e** VSe_2-thickness-dependent Γ of the optical transition estimated by model fitting based on Eq. (4). **f** Dynamic evolution of TR signals in Bi_2Se_3 and VBHs. The gray fit curves indicate biexponential decays in Bi_2Se_3 and VBHs with 48 nm and 118 nm VBH. Inset: VSe_2-thickness-dependent interband recombination time of metastable carrier in Bi_2Se_3 (τ_2). The error bars in (**d**), (**e**), and the inset of (**f**) indicate the standard error of the fitted values in (b).

spectra can be derived from the change of complex refractive index, which is closely related to the change of absorption coefficient as explained by the Kramers–Kronig relation. Accordingly, we fitted our experimentally observed TR spectra by taking into account the pump-induced refractive index changes of bulk band Bi_2Se_3 (details in Experimental Methods). This model provides information on the optical transition in Bi_2Se_3 such as the transition energy (E_{opt}) and phenomenological broadening factor (Γ). The fit results of TR spectra at 25 ps are displayed in Fig. 4b and their photoinduced absorption changes ($\Delta\alpha$) in Fig. 4c with the optical transition energy of $E_{opt} = 0.96$ eV and the broadening factor of $\Gamma = 45$ meV. The calculated absorption coefficient was subsequently confirmed by the transient absorption (TA) spectra and well matched with the measured result as shown in Figs. S3b, c. According to the fitting model, an assumption of photoexcited carrier concentration (n_{ex}) of 9.7×10^{18} cm^{-3}, which is only ~3% of the background carrier concentration (N_0), provided the best fit of the spectral response at 25 ps. We note that the photoexcited carrier concentration of 9.7×10^{18} cm^{-3} well matched the estimated value of 1.6×10^{19} cm^{-3} from the complex refractive index of Bi_2Se_3 and optical power density, but was slightly small due to carrier recombination. In addition, the second surface states (SS_2) locate about 1.5 eV above the first conduction band (CB_1) edge[64]. Therefore, the pump beam ($\hbar\omega_{pump}$= 1.5 eV) can directly excite 2D electrons in SS2 from the CB and 3D carriers from a deep level of VB to CB_1 band[64,65]. The latter density of optical transition was expected to be dominant[65]. Then, the probe energy (~0.8−1.1 eV) can be coupled with the optical transitions between SS_1-SS_2 and discrete bulk bands. Subsequently, a non-resonant TR signal at SS_1–SS_2 transitions and a resonant TR signal at discrete bulk bands can be expected. Therefore, the obtained transition energy of 0.96 eV with the derivative TR implied that the TR response originated from the pump-induced absorption between the first and second conduction bands (CB_1–CB_2) in Bi_2Se_3[66]. The obtained transition energy of 0.96 eV agreed well with the previous results of the bulk band in Bi_2Se_3[66,67].

In the VBHs with 48, 57, 118, and 167 nm thick VSe_2, the changes of the spectral and dynamical response of Bi_2Se_3 were observed according to VSe_2 thickness as shown in Fig. 4a, b. A notable change is that the derivative-like TR of Bi_2Se_3 feature was redshifted with increasing thickness of VSe_2, as indicated by the horizontal line in Fig. 4a and the asymmetry TR spectra (larger negative $\Delta R/R_0$ than positive $\Delta R/R_0$) became severe with increasing VSe_2 thickness (Fig. 4b). This asymmetric behavior of the TR spectra in the VBHs originated from the TR component of VSe_2, which remained almost constant (Fig. 3a and Figs. S4c).

We took the TR response of VSe_2 into account as a constant value during the model fitting process. Further details of TR spectrum modeling in VBHs can be found in the Experimental Methods section. The fitting result with our theoretical model provides the E_{opt} and Γ of photoinduced absorption changes in the VBHs as shown in Fig. 4c. The magnitude of $\Delta\alpha$ is significantly increased in VBHs (~2.5 times in 167 nm VBH), which is consistent with the results shown in Fig. 3b as the larger excited carrier density (n_{ex}) by transferring from VSe_2 to Bi_2Se_3. E_{opt} shows a linear dependence on the thickness of VSe_2 with the slope of 0.26 meV nm^{-1} (Fig. 4d). The factor of Γ also tends to increase with the thickness of VSe_2 (Fig. 4e). Figure 4f shows the decay characteristics of photoexcited carriers in the VBHs. In Bi_2Se_3, the pump–probe trace followed a biexponential decay. τ_1 and τ_2 indicate the decay times related to the electron-LO (longitudinal-optical) phonon relaxation and the interband relaxation involving unoccupied DSS, respectively[38,68]. The intraband relaxation by electron-LO phonon scattering is typically obtained with values of decay constants from 1 to 3 ps range, due to low LO-phonon energy and electron–phonon coupling in Bi_2Se_3. τ_1 decay time in Bi_2Se_3 and VBHs were measured to be in the range of 1–3 ps, implying intrinsic elastic and electron–phonon coupling properties of Bi_2Se_3 regardless of VSe_2. However, τ_2 related to the interband relaxation including DSS was observed in a much longer decay time range. Compared to the longer decay time (τ_2 ~ 600 ps) in Bi_2Se_3 thin film, τ_2 in VBHs was significantly shortened (see Supplementary Fig. 5). The fast relaxation in VBH indicates the efficient interband carrier recombination including coupling with DSS[68], owing to the depletion of 3D carriers and stabilized 2D electrons by charge transfer after junction with VSe_2.

Such spectral and dynamical changes of derivative TR spectra of the insulating bulk band suggest interactions between metallic VSe_2 and conduction/valence bands in Bi_2Se_3 by forming junctions. Accordingly, this section mainly handles the electronic interaction between the insulating bulk band of Bi_2Se_3 and metallic VSe_2, which provides a good example of van der Waals MSJs. Previous ultrafast spectroscopic studies show that the interesting features in MSJ are determined by the interface[33,69,70]. Generally, certain changes in the electronic states of the semiconductor in MSJs can be explained by metal/defect-induced gap states (MIGS, DIGS), or interfacial dipoles that cause the FLP observed in different MSJs[20,21]. Since the MIGS store the electrons and holes and then pin the Fermi level, they can modulate the carrier dynamics of Bi_2Se_3. However, this can be sufficiently suppressed in the case of vdW MSJs owing to the vdW interaction[18–21]. Although DIGS can also affect the carrier responses, similar to MIGS, they are negligible in the present work due to the verified high-quality interface. Most noteworthy is that both MIGS and DIGS, due to the overlap of wave functions occurring at the MS interface, are independent of the thickness of the contact metal. Consequently, the observed VSe_2-thickness-dependent redshift of transition energy suggests that the bulk band modulation can be much better interpreted by interfacial dipole interaction rather than MIGS and DIGS in MSJ.

In the case of interfacial dipoles due to charge transfer and redistribution, they can shift the electronic level, deviating from the Schottky–Mott limit[71,72]. Fig. 5a illustrates the band alignment of VSe_2 and Bi_2Se_3 after contact. Due to the low χ (~5.3 eV) and small bulk bandgap (E_g ~ 0.3 eV) in Bi_2Se_3 compared to the W of VSe_2 (~5.8 eV), electrons are transferred from Bi_2Se_3 to VSe_2 due to the Fermi level alignment after contact (Fig. 5a). Subsequently, the VSe_2 layer close to the interface becomes negatively charged, while positive charges are created in the Bi_2Se_3 layer close to the interface, leading to interfacial dipoles (Fig. 5a). These interfacial dipoles due to charge transfer lift the electronic level of Bi_2Se_3 layers near the interface, whereas the Bi_2Se_3 layers far from the interface remain unchanged due to the rapid decay with distance from the interface[71,72]. With this modulation, a band offset (Δ) is created as displayed in Fig. 5a. We note that the photoinduced built-in electric field is negligible at the interface of the MSJ in our experiment due to a small perturbation of ~3% of background carrier density. Hence, dipole interactions are dominant, which enables us to estimate the Δ (= $E_{opt,VBH}$ − $E_{opt,Bi2Se3}$) created by the junction with metallic VSe_2. The redshift of the optical transition energy in the VBHs makes it possible to move the transitions of CB_1–CB_2 to promoted by Δ. Thus, the observed transition energy directly reflects the Δ induced by the interfacial dipole interaction with the electronic level of Bi_2Se_3. Moreover, the upward bending in the electronic level of Bi_2Se_3 layers with increasing VSe_2 thickness in VBH also resulted in the increasing broadening factor of the projected Bi_2Se_3 band structure as shown in Fig. 4e. The effect through the interfacial dipole interaction depends on the thickness of the metallic contact layer because more electrons require severer Fermi level alignment with increasing VSe_2 thickness, and thus, the dipole strength becomes stronger (Fig. 5a). Particularly, in the 167 nm thick VBH (dashed box in Fig. 4a), the observed additional optical transition over 1 eV reflects the highly distorted electronic level due to strong dipole interactions. Note that the electronic level shift of Bi_2Se_3 by the junction with VSe_2 was ~10 times lower compared to conventional 3D metals[11], including Au, Pd, and Pt. This implies that extremely weak interactions can be achieved with VSe_2 as the 2D metal electrode.

The estimated Δ showed a linear dependence on the thickness of VSe_2 with a slope of 0.26 meV nm^{-1} (Fig. 5b). The Δ on the order of several tenths of meV is comparable to the order of the first-principles calculation result for metal-2D semiconductor junctions[72]. Moreover, observed VSe_2-thickness-dependent electronic level shift (Δ) in Bi_2Se_3 suggests that Δ becomes almost zero with monolayer VSe_2, expecting extrapolation in Fig. 5b. This interpretation is consistent with the recent angle-resolved photoemission spectroscopy (ARPES) study of monolayer VSe_2/Bi_2Se_3 heterostructures[73], which directly observe the unchanged band structure and no band bending of Bi_2Se_3 under VSe_2 monolayer (0.3–2 ML). Since Φ_{SB} is determined by the energy difference between the conduction band edges and the Fermi level in Bi_2Se_3 ($\Phi_{SB} = E_{CBM}$-E_F) for electrons, the $\triangle$ observed from their inherent levels leads to a deviation from the Schottky–Mott limit ($S = 1$)[21,71,72]. The pinning factor S, which is defined as $S = 1 - \Delta/\Phi_{SB,0}$, where $\Phi_{SB,0}$ is the SBH in non-interacting subsystem and denotes the strength of FLP, which is deduced from the estimated Δ (Fig. 5c). Note that S became closer to the Schottky–Mott limit as the thickness of VSe_2 decreased. Consequently, the changes in the SBH due to charge transfer and interfacial dipoles are expected to be weak in vdW MSJs with an ultrathin layer (monolayer to few-layer), and further approaching the ideal Schottky–Mott limit ($S = 1$) is possible. The broadening factor of the optical transition in Bi_2Se_3 also increased with the increasing thickness of the VSe_2 layer (Fig. 4e). The gradual shift of the electronic bands in the Bi_2Se_3 layers reflects that the width of the optical transition in Bi_2Se_3 is broadened in the projected band structure, as illustrated in Fig. 5a. This trend was also observed in previous studies on electronic band modulation under an external electric field[74–76]. Moreover, since the lifetime of metastable carriers (τ_2) strongly depends on the Fermi level of Bi_2Se_3[39,40], strong FLP can pin the τ_2 regardless of VSe_2 thickness. Accordingly, significant VSe_2-thickness-dependence of τ_2 shows additional evidence of weak FLP, originated by interfacial hybridization or defect states. On the other side, the interband recombination time of metastable carriers decreased with increasing Δ, owing to the stronger interfacial dipole interaction. The electrons and holes contributed

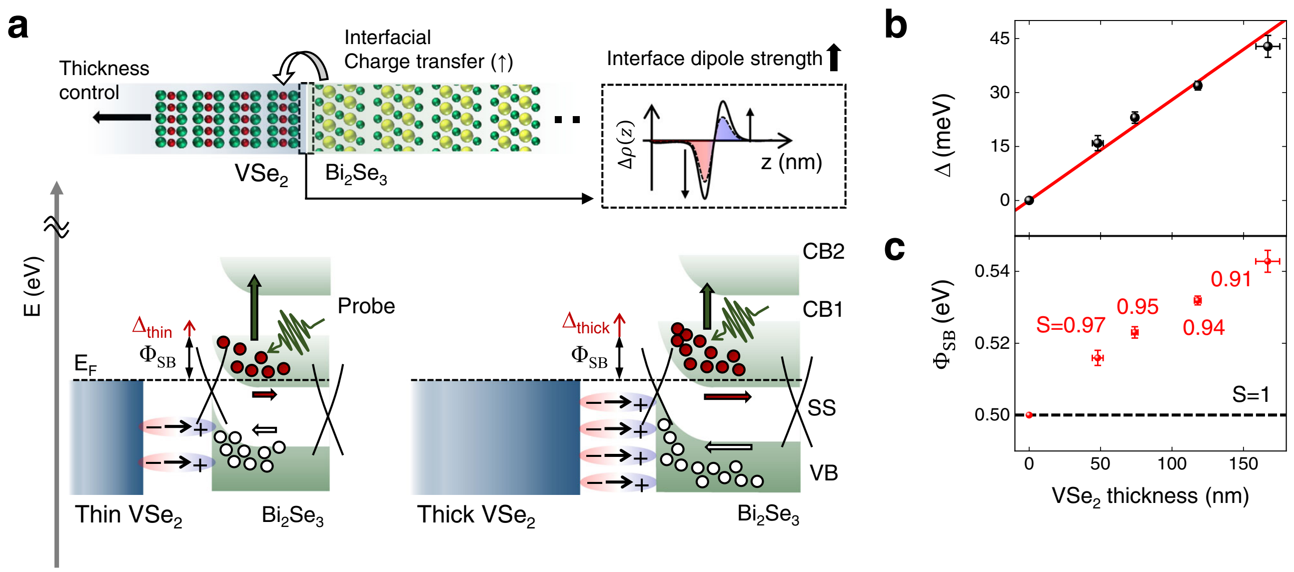

Fig. 5 Schematic of changes of the VSe2-thickness-dependent optical transition behavior in VBHs after contact with VSe2. a Schematic of charge transfer and redistribution due to the thermal equilibrium by the junction at VSe_2/Bi_2Se_3 and corresponding charge density near the junction interface. The increase of VSe_2 thickness requires a larger amount of electron from Bi_2Se_3 for Fermi level alignment, leading to an increase of the interfacial dipole strength. Corresponding band diagram for VSe_2/Bi_2Se_3 junctions with thin and thick VSe_2 are illustrated with the electron Schottky barrier height (SBH, Φ_{SB}) and band offset (△) as indicated by black and red vertical arrows, respectively. The CB1/CB2, VB, and SS imply the first/second conduction band, valence band, and surface state of Bi_2Se_3, respectively. The green vertical arrow indicates optical transitions corresponding to probe energies. **b** VSe_2-thickness-dependent band offset (△) by dipole interactions and **c** estimated electron Φ_{SB}. The expected pinning factor S is listed. The error bars in (**b**) and (**c**) come from the standard error for fitted values of E_{opt} in Fig. 4d.

to the surface recombination in band edges and DSS enables the current to flow efficiently (Fig. 5a). Then, it becomes possible for the metastable carriers of Bi_2Se_3 to flow efficiently to each surface, giving rise to the shortening of the metastable carrier lifetime (Fig. 4f). This result is consistent with the observed redshift of the transition energy and broadening of the optical transition and shows good agreement with previous reports on exciton dissociation mechanisms, which were previously studied in 2D semiconductors with in-plane dissociation of strongly bound exciton under an external electric field[74] and out-of-plane dissociation due to the built-in-field of the p–n doping[77].

Conclusion

In summary, by employing ultrafast spectroscopy, we investigated the interfacial carrier dynamics in both of metallic surface state and insulating bulk state in VSe_2/Bi_2Se_3, for which a nearly perfect interface was realized and the dependence of the dipole effect hidden by MIGS and DIGS on the metal thickness was observed. The excellent interfacial contact in the MSJs was verified by precise STEM images and interfacial CAP dynamics. The hot electron transfer from VSe_2 to Bi_2Se_3 across vdW gap in ultrashort timescale (~100 fs) before thermalization in VSe_2 enables to improve the efficiency of Bi_2Se_3-based optoelectronic devices. Furthermore, it was found that the metallic surface state of Bi_2Se_3 was well preserved even after contact with VSe_2. The VSe_2thickness-dependent TR measurements quantitatively provided electronic level shifts of the bulk band in Bi_2Se_3 due to dipole interactions, leading to deviation from the Schottky–Mott limit. In addition, the observed carrier long-decay characteristics in VBHs show a strong dependence on the VSe_2 thickness and there were no significant FLP effects. The metastable carrier lifetime was noticeably shorter due to the built-in field, enabling a highly efficient current flow of Bi_2Se_3-based devices.

Our results show that VSe_2 is a promising candidate as the 2D metal electrode for diverse applications based on Bi_2Se_3 and other topological insulators. Moreover, the interfacial dipole interaction created by charge transfer and redistribution allows us to understand the carrier dynamics and modulated electronic states in MSJs, approaching the ideal Schottky–Mott limit. Although thickness control of the semiconductor part in MSJs has been suggested to cover the effects of interfacial dipoles due to the depinning effect between the semiconductor layers, i.e., a multilayer (thick) semiconductor is an advantageous option for suppressing FLP[71,72], the practical development remains elusive due to the significant changes in the electrical and optical properties from the monolayer counterpart. Thus, the combination of defining an approach to perceive the modulated band structures in MSJs that may encompass delicate materials and finding suitable vdW materials close to the ideal junctions shown in the present work provides a strategy for the contact fabrication process for optimizing device performance by fully utilizing the intrinsic properties of Bi_2Se_3 and other topological insulators.

Methods

Fabrication of VSe_2/Bi_2Se_3 heterostructures. A Bi_2Se_3 thin film was grown by a molecular beam epitaxy system with an ultrahigh vacuum chamber equipped with VEECO (Knudsen) cells of high purity bismuth (99.999+%) and selenium (99.999%) sources[78]. Prior to growth, the Al_2O_3 (001) substrate was cleaned with acetone and isopropyl alcohol and baked at 700 °C for 30 min to remove any residual contaminants. A Bi_2Se_3/Al_2O_3 (001) film was grown at 250 °C for 90 min, followed by a post-annealing process of 450 °C for 30 min for self-crystallization. The ratio of Bi and Se fluxes was kept at ~1:15 to minimize Se vacancies. The formation of crystalline Bi_2Se_3 on the substrate was monitored by an in situ reflections high-energy electron diffraction system. The carrier concentration was determined by Hall resistivity measurement at 300 K. The carrier concentration (N_0) of Bi_2Se_3 is given by $N_0 = (B{\cdot}I)/(e{\cdot}d{\cdot}V_H)$, where I is current, d is the thickness of the Bi_2Se_3 thin film, e is the electron charge, and V_H is the Hall voltage; thus, we can estimate $N_0 = 3.13 \times 10^{20}\,\mathrm{cm}^{-3}$.

Single-crystalline 1T-VSe_2 was grown by the chemical vapor transport method[41]. V (99.5% purity) and Se (99.999% purity) powders were used as the precursors with a stoichiometric amount of 2:1 wt%. As a transport agent (concentration of 1.5 mg/cm^3), VCl_3 powder (99% purity) was used to provide sufficient vapor pressure. The mixture of precursors and transport agents was placed in a quartz ampule. The ampule was evacuated below 10^{-6} Torr, followed by melting and sealing. The sealed quartz ampule was placed at the center between two heating zones, which were heated slowly in five steps to approach their target temperatures (750 °C for vaporization and 850 °C for growth). After being held for 72 h at the maximum temperatures, the system was cooled down naturally, and shiny silver-gray VSe_2 crystals were collected after breaking the ampule.

We adopted mechanical exfoliation to transfer VSe_2 onto Bi_2Se_3 for the fabrication of VSe_2/Bi_2Se_3 heterostructures. VSe_2 flakes were transferred onto the Bi_2Se_3 thin film by using a simple blue tape method. We selected one of them, and different thicknesses were exposed on one VSe_2 flake for a consistent experimental environment.

Characterization of VSe_2/Bi_2Se_3 heterostructures. The thickness of the VSe_2 flake was analyzed by AFM (n-Tracer, Nano Focus Inc.) operated in a non-contact mode. Raman measurements were performed with a Raman spectrometer (FEX, NOST) by focusing the laser radiation with a 0.3 mW power centered at 531 nm. A microstructural study was carried out using a STEM system (JEM-ARM200F, JEOL) equipped with a probe spherical aberration corrector. HAADF-STEM images were obtained to confirm the atomic structure in real space. For HAADF-STEM images, the convergent semiangle was fixed at 22 mrad, and the collection semiangle was 67–170 mrad. TEM specimens were thinned for electron transparency by a focused ion beam system.

Transient reflectance (TR) measurements. CAP dynamics and TR measurements were performed by employing a Ti:sapphire laser oscillator (MAITAI, Spectra-Physics), which produced 100-fs pump pulses at an 80-MHz repetition rate. The main portion of the output from the oscillator at a central wavelength of 830 nm was further used to pump a synchronously pumped optical parametric oscillator (SPOPO) for the generation of tuneable 150-fs probe pulses (1150–1550 nm) at the same repetition rate. With a dichroic mirror, the pump and probe pulses were collinearly combined and focused on the sample to a beam waist of ~2 μm by a single objective lens (M Plan Apo 100×, Mitutoyo). The pump fluence adjusted with two polarizers was ~12 $\mu J/cm^2$. The time delay between the pump and probe pulses was controlled by using a motorized linear stage. The reflected probe beam was recorded with a Ge photodetector (DET50B, Thorlabs) connected to a lock-in amplifier (SR830, Stanford Research Systems) after blocking the reflected pump beams. Based on this setup, we measured the time-resolved differential reflectance defined by $\Delta R/R_0 \equiv (R_0 - R(t))/R_0$ where R_0 and $R(t)$ are the reflectance of the sample without and with pump excitation, respectively. All measurements were carried out under ambient conditions at room temperature.

Modeling of TR spectra. The theoretical model for analyzing the TR feature is based on pump-induced refractive index changes for semiconducting materials[34]. The pump pulses excite electrons in that ground state, then perturb the dielectric response and fractionally change the complex refractive index of $\widetilde{n} = n + ik$. First, we calculated the imaginary part of k corresponding to absorption coefficient as $k = (\lambda/4\pi)\alpha$, where λ is the probe wavelength and α is the absorption coefficient. Once the change of absorption coefficient ($\Delta\alpha$) is obtained, the change of real part of the refractive index ($\triangle n$) is derived by using the Kramers–Kronig transformation

$$\Delta n(\hbar\omega) = \frac{\hbar c}{\pi} P \int_0^\infty \frac{\Delta\alpha(\hbar\omega)}{\omega'^2 - \omega^2}\, \mathrm{d}\omega\prime \tag{2}$$

where c is the speed of light, and P is the Cauchy principal value for the integral. We calculated the absorption coefficient change with optical absorption of $\delta(\hbar\omega_{\mathrm{opt}})$ with perturbed factor as photoexcited carrier concentration divided by doping concentration ($\Delta N/N_0$) and with homogeneous broadening by deconvolution with Gaussian function. The broadening factor Γ is included in the calculation.

In the measurement, since the observed fractional reflectance change ($\Delta R/R_0$) was too small ($\sim 10^{-4}$) by normal incident pump pulses, the observed differential reflectance was dominated by refractive index changes. From this, $\Delta R/R_0$ can be approximated as

$$\frac{\Delta R}{R_0}(\hbar\omega) \approx \left(\frac{4}{n(\hbar\omega)^2 - 1}\right) \cdot \triangle n(\hbar\omega) \tag{3}$$

where $n_0 = 5.5$ is the averaged refractive index of Bi_2Se_3 in the interesting spectral region[50]. To obtain the optical transition energy and broadening factor in VBHs, we performed the model fit in TR spectra of VBH at the same time delay of 25 ps. In Bi_2Se_3, asymmetrical positive and negative peaks in TR spectra were observed as displayed in Supplementary Notes 2, 3. However, in VBHs, the asymmetrical TR spectra were observed with small positive peaks at lower energy and large negative peaks at higher energy as can be seen in Fig. 4b. Subsequently, we modified the Eq. (3) for TR spectra in VBHs as

$$\frac{\Delta R}{R_0}(\hbar\omega) \approx \left(\frac{4}{n(\hbar\omega)^2 - 1}\right) \cdot \Delta n(\hbar\omega) + C_{\mathrm{VSe_2}} \tag{4}$$

where $C_{\mathrm{VSe_2}}$ is the constant TR response of the bare VSe_2 as shown in Supplementary Fig. 4c. The value of $C_{\mathrm{VSe_2}}$ became larger with the increase of VSe_2 thickness and is consistent with the modified model of TR response in VBHs.

Data availability

The data of this work are available from the corresponding authors upon request.

Code availability

The code that supports the findings of this study are available from the corresponding author upon reasonable request.

Received: 27 December 2021; Accepted: 1 July 2022;
Published online: 14 July 2022

References

1. Moore, J. E. The birth of topological insulators. *Nature* **464**, 194–198 (2010).
2. Hasan, M. Z. & Kane, C. L. Colloquium: topological insulators. *Rev. Mod. Phys.* **82**, 3045 (2010).
3. Pesin, D. & MacDonald, A. H. Spintronics and pseudospintronics in graphene and topological insulators. *Nat. Mater.* **11**, 409–416 (2012).
4. Vandenberghe, W. G. & Fischetti, M. V. Imperfect two-dimensional topological insulator field-effect transistors. *Nat. Commun.* **8**, 1–8 (2017).
5. Zhang, Q., Iannaccone, G. & Fiori, G. Two-dimensional tunnel transistors based on Bi_2Se_3 thin film. *IEEE Electron Device Lett.* **35**, 129–131 (2013).
6. McIver, J., Hsieh, D., Steinberg, H., Jarillo-Herrero, P. & Gedik, N. Control over topological insulator photocurrents with light polarization. *Nat. Nanotechnol.* **7**, 96–100 (2012).
7. Huang, S. & Xu, X. Optical chirality detection using a topological insulator transistor. *Adv. Opt. Mater.* **9**, 2002210 (2021).
8. Zhang, H., Zhang, X., Liu, C., Lee, S.-T. & Jie, J. High-responsivity, high-detectivity, ultrafast topological insulator Bi_2Se_3/silicon heterostructure broadband photodetectors. *ACS Nano* **10**, 5113–5122 (2016).
9. Wang, F. et al. Submillimeter 2D Bi_2Se_3 flakes toward high-performance infrared photodetection at optical communication wavelength. *Adv. Funct. Mater.* **28**, 1802707 (2018).
10. Mellnik, A. et al. Spin-transfer torque generated by a topological insulator. *Nature* **511**, 449–451 (2014).
11. Spataru, C. D. & Léonard, F. Fermi-level pinning, charge transfer, and relaxation of spin-momentum locking at metal contacts to topological insulators. *Phys. Rev. B* **90**, 085115 (2014).
12. Walsh, L. A. et al. Interface chemistry of contact metals and ferromagnets on the topological insulator Bi_2Se_3. *J. Phys. Chem. C* **121**, 23551–23563 (2017).
13. Yeh, Y.-C. et al. Growth of the Bi_2Se_3 surface oxide for metal–semiconductor–metal device applications. *J. Phys. Chem. C* **120**, 3314–3318 (2016).
14. Cho, S., Butch, N. P., Paglione, J. & Fuhrer, M. S. Insulating behavior in ultrathin bismuth selenide field effect transistors. *Nano Lett.* **11**, 1925–1927 (2011).
15. Lang, M. et al. Revelation of topological surface states in Bi_2Se_3 thin films by in situ Al passivation. *ACS Nano* **6**, 295–302 (2012).
16. Xu, S. et al. van der Waals epitaxial growth of atomically thin Bi_2Se_3 and thickness-dependent topological phase transition. *Nano Lett.* **15**, 2645–2651 (2015).
17. Kim, C. et al. Fermi level pinning at electrical metal contacts of monolayer molybdenum dichalcogenides. *ACS Nano* **11**, 1588–1596 (2017).
18. Wang, Y. et al. Van der Waals contacts between three-dimensional metals and two-dimensional semiconductors. *Nature* **568**, 70–74 (2019).
19. Allain, A., Kang, J., Banerjee, K. & Kis, A. Electrical contacts to two-dimensional semiconductors. *Nat. Mater.* **14**, 1195–1205 (2015).
20. Liu, Y. et al. Approaching the Schottky–Mott limit in van der Waals metal–semiconductor junctions. *Nature* **557**, 696–700 (2018).
21. Liu, Y., Stradins, P. & Wei, S.-H. Van der Waals metal-semiconductor junction: Weak Fermi level pinning enables effective tuning of Schottky barrier. *Sci. Adv.* **2**, e1600069 (2016).
22. Shen, T., Ren, J.-C., Liu, X., Li, S. & Liu, W. van der Waals stacking induced transition from Schottky to ohmic contacts: 2D metals on multilayer InSe. *J. Am. Chem. Soc.* **141**, 3110–3115 (2019).
23. Liu, Y. et al. Toward barrier free contact to molybdenum disulfide using graphene electrodes. *Nano Lett.* **15**, 3030–3034 (2015).
24. Chuang, H.-J. et al. High mobility WSe_2 *p*-and *n*-type field-effect transistors contacted by highly doped graphene for low-resistance contacts. *Nano Lett.* **14**, 3594–3601 (2014).

25. Chee, S. S. et al. Lowering the Schottky barrier height by graphene/Ag electrodes for high-mobility MoS_2 field-effect transistors. *Adv. Mater.* **31**, 1804422 (2019).
26. Zhao, B. et al. 2D Metallic Transition-metal dichalcogenides: structures, synthesis, properties, and applications. *Adv. Funct. Mater.* **31**, 2105132 (2021).
27. Zhang, Z. et al. Van der Waals epitaxial growth of 2D metallic vanadium diselenide single crystals and their extra-high electrical conductivity. *Adv. Mater.* **29**, 1702359 (2017).
28. Shi, J. et al. Two-dimensional metallic vanadium ditelluride as a high-performance electrode material. *ACS Nano* **15**, 1858–1868 (2021).
29. Ji, Q. et al. Metallic vanadium disulfide nanosheets as a platform material for multifunctional electrode applications. *Nano Lett.* **17**, 4908–4916 (2017).
30. Zhang, Z. et al. Epitaxial growth of two-dimensional metal–semiconductor transition-metal dichalcogenide vertical stacks (VSe_2/MX_2) and their band alignments. *ACS Nano* **13**, 885–893 (2018).
31. Ci, H. et al. Defective VSe_2-graphene heterostructures enabling in situ electrocatalyst evolution for lithium–sulfur batteries. *ACS Nano* **14**, 11929–11938 (2020).
32. Yang, C. et al. Metallic graphene-like VSe_2 ultrathin nanosheets: superior potassium-ion storage and their working mechanism. *Adv. Mater.* **30**, 1800036 (2018).
33. Yang, Y. et al. Semiconductor interfacial carrier dynamics via photoinduced electric fields. *Science* **350**, 1061–1065 (2015).
34. Yang, Y. et al. Low surface recombination velocity in solution-grown $CH_3NH_3PbBr_3$ perovskite single crystal. *Nat. Commun.* **6**, 1–6 (2015).
35. Zhong, C. et al. Hot carrier and surface recombination dynamics in layered InSe crystals. *J. Phys. Chem. Lett.* **10**, 493–499 (2019).
36. Wu, L. et al. A sudden collapse in the transport lifetime across the topological phase transition in $(Bi_{1-x}In_x)_2Se_3$. *Nat. Phys.* **9**, 410–414 (2013).
37. Glinka, Y. D. et al. Ultrafast carrier dynamics in thin-films of the topological insulator Bi_2Se_3. *Appl. Phys. Lett.* **103**, 151903 (2013).
38. Glinka, Y. D., Li, J., He, T. & Sun, X. W. Clarifying ultrafast carrier dynamics in ultrathin films of the topological insulator Bi_2Se_3 using transient absorption spectroscopy. *ACS Photon.* **8**, 1191–1205 (2021).
39. Luo, C.-W. et al. Snapshots of Dirac fermions near the Dirac point in topological insulators. *Nano Lett.* **13**, 5797–5802 (2013).
40. Sim, S. et al. Picosecond competing dynamics of apparent semiconducting-metallic phase transition in the topological insulator Bi_2Se_3. *ACS Photon.* **7**, 759–764 (2020).
41. Feroze, A. et al. In-depth structural characterization of 1T-VSe_2 Single crystals grown by chemical vapor transport. *Cryst. Growth Des.* **20**, 2860–2865 (2020).
42. Zhao, Y. et al. Interlayer vibrational modes in few-quintuple-layer Bi_2Te_3 and Bi_2Se_3 two-dimensional crystals: Raman spectroscopy and first-principles studies. *Phys. Rev. B* **90**, 245428 (2014).
43. Li, D. et al. Structural phase transition of multilayer VSe_2. *ACS Appl. Mater. Interfaces* **12**, 25143–25149 (2020).
44. Park, T. G. et al. Coherent control of interlayer vibrations in Bi_2Se_3 van der Waals thin-films. *Nanoscale* **13**, 19264–19273 (2021).
45. Greener, J. D. et al. Coherent acoustic phonons in van der Waals nanolayers and heterostructures. *Phys. Rev. B* **98**, 075408 (2018).
46. Glinka, Y. D., Babakiray, S., Johnson, T. A., Holcomb, M. B. & Lederman, D. Acoustic phonon dynamics in thin-films of the topological insulator Bi_2Se_3. *J. Appl. Phys. Lett.* **117**, 165703 (2015).
47. Wang, H., Xu, Y., Shimono, M., Tanaka, Y. & Yamazaki, M. Computation of interfacial thermal resistance by phonon diffuse mismatch model. *Mater. Trans.* **48**, 2349–2352 (2007).
48. Gospodarev, I. et al. Elastic properties and phonon spectra of quasi-two-dimensional VSe_2. *Low Temp. Phys.* **29**, 151–154 (2003).
49. Wen, Y.-C. et al. Specular scattering probability of acoustic phonons in atomically flat interfaces. *Phys. Rev. Lett.* **103**, 264301 (2009).
50. McIver, J. et al. Theoretical and experimental study of second harmonic generation from the surface of the topological insulator Bi_2Se_3. *Phys. Rev. B* **86**, 035327 (2012).
51. Sobota, J. A. et al. Ultrafast optical excitation of a persistent surface-state population in the topological insulator Bi_2Se_3. *Phys. Rev. Lett.* **108**, 117403 (2012).
52. Sim, S. et al. Ultrafast terahertz dynamics of hot Dirac-electron surface scattering in the topological insulator Bi_2Se_3. *Phys. Rev. B* **89**, 165137 (2014).
53. Srishti, P. et al. Pressure-induced 1*T* to 3*R* structural phase transition in metallic VSe_2: X-ray diffraction and first-principles theory. *Phys. Rev. B* **104**, 014108 (2021).
54. He, J., Xie, Q. & Xu, G. Confinement effect enhanced Stoner ferromagnetic instability in monolayer 1T-VSe_2. *N. J. Phys.* **23**, 023027 (2021).
55. Guo, L. & Xu, X. Ultrafast spectroscopy of electron-phonon coupling in gold. *J. Heat. Transf.* **136**, 122401 (2014).
56. Dawlaty, J. M., Shivaraman, S., Chandrashekhar, M., Rana, F. & Spencer, M. G. Measurement of ultrafast carrier dynamics in epitaxial graphene. *Appl. Phys. Lett.* **92**, 042116 (2008).
57. Nakamura, A., Shimojima, T., Nakano, M., Iwasa, Y. & Ishizaka, K. Electron and lattice dynamics of transition metal thin films observed by ultrafast electron diffraction and transient optical measurements. *Struct. Dyn.* **3**, 064501 (2016).
58. Block, A. et al. Tracking ultrafast hot-electron diffusion in space and time by ultrafast thermomodulation microscopy. *Sci. adv.* **5**, eaav8965 (2019).
59. Park, T. G. et al. Interlayer coupling and ultrafast hot electron transfer dynamics in metallic VSe_2/graphene van der Waals heterostructures. *ACS Nano* **15**, 7756–7764 (2021).
60. He, J. et al. Electron transfer and coupling in graphene–tungsten disulfide van der Waals heterostructures. *Nat. Commun.* **5**, 1–5 (2014).
61. Yuan, L. et al. Photocarrier generation from interlayer charge-transfer transitions in WS_2-graphene heterostructures. *Sci. Adv.* **4**, e1700324 (2018).
62. Claessen, R., Schafer, I. & Skibowski, M. The unoccupied electronic structure of 1T-VSe_2. *J. Phys.: Condens. Matter* **2**, 10045 (1990).
63. Brahlek, M., Kim, Y. S., Bansal, N., Edrey, E. & Oh, S. Surface versus bulk state in topological insulator Bi_2Se_3 under environmental disorder. *Appl. Phys. Lett.* **99**, 012109 (2011).
64. Sobota, J. A. et al. Direct optical coupling to an unoccupied Dirac surface state in the topological insulator Bi_2Se_3. *Phys. Rev. Lett.* **111**, 136802 (2013).
65. Zhu, L.-G., Kubera, B., Fai Mak, K. & Shan, J. Effect of surface states on terahertz emission from the Bi_2Se_3 surface. *Sci. Rep.* **5**, 1–8 (2015).
66. Zhang, H. et al. Topological insulators in Bi_2Se_3, Bi_2Te_3 and Sb_2Te_3 with a single Dirac cone on the surface. *Nat. Phys.* **5**, 438–442 (2009).
67. Lawal, A. & Shaari, A. Density functional theory study of electronic properties of Bi_2Se_3 and Bi_2Te_3. Mal. J. Fun*d. Appl. Sci.* **12** (2016).
68. Glinka, Y. D., Babakiray, S., Johnson, T. A., Holcomb, M. B. & Lederman, D. Effect of carrier recombination on ultrafast carrier dynamics in thin films of the topological insulator Bi_2Se_3. *Appl. Phys. Lett.* **105**, 171905 (2014).
69. Lee, K. et al. Sub-picosecond carrier dynamics induced by efficient charge transfer in $MoTe_2/WTe_2$ van der Waals heterostructures. *ACS Nano* **13**, 9587–9594 (2019).
70. Seo, D. M. et al. Ultrafast excitonic behavior in two-dimensional metal–semiconductor heterostructure. *ACS Photon.* **6**, 1379–1386 (2019).
71. Wang, Q., Shao, Y. & Shi, X. Mechanism of charge redistribution at the metal–semiconductor and semiconductor–semiconductor interfaces of metal–bilayer MoS_2 junctions. *J. Chem. Phys.* **152**, 244701 (2020).
72. Wang, Q., Shao, Y., Gong, P. & Shi, X. Metal–2D multilayered semiconductor junctions: layer-number dependent Fermi-level pinning. *J. Mater. Chem. C.* **8**, 3113–3119 (2020).
73. Yilmaz, T. et al. Emergent flat band electronic structure in a VSe_2/Bi_2Se_3 heterostructure. *Commun. Mater.* **2**, 1–8 (2021).
74. Massicotte, M. et al. Dissociation of two-dimensional excitons in monolayer WSe_2. *Nat. Commun.* **9**, 1–7 (2018).
75. Zhang, L. et al. Quantum-confined stark effect in the ensemble of phase-pure CdSe/CdS quantum dots. *Nanoscale* **11**, 12619–12625 (2019).
76. Park, K., Deutsch, Z., Li, J. J., Oron, D. & Weiss, S. Single molecule quantum-confined Stark effect measurements of semiconductor nanoparticles at room temperature. *ACS Nano* **6**, 10013–10023 (2012).
77. Riis-Jensen, A. C., Pandey, M. & Thygesen, K. S. Efficient charge separation in 2D Janus van der Waals structures with built-in electric fields and intrinsic *p–n* doping. *J. Phys. Chem. C* **122**, 24520–24526 (2018).
78. Jerng, S.-K., Jeon, J. H., Kim, Y., Kim, J. S. & Chun, S.-H. Multiple surface conduction channels via topological insulator and amorphous insulator thin film multi-stacks. *Curr. Appl. Phys.* **19**, 219–223 (2019).

Acknowledgements

This work was supported by the National Research Foundation of Korea (NRF) funded by the Korean Government (2019R1A2C3003504, 2020R1A4A2002828). J.H.J. and S.-H.C. acknowledge the support from the NRF grant (2016R1E1A1A01942649). S.L. acknowledges the support from the NRF grant (2021R1F1A1050726).

Author contributions

T.G.P., S.L., and F.R. conceived the original idea. J.H.J., S.-H.C., and S.L. synthesized and characterized the VSe_2/Bi_2Se_3 heterostructure samples. T.G.P. performed the time-resolved experiments and data analysis. T.G.P. S.L., and F.R. discussed the results. F.R. supervised the project. T.G.P., S.L., and F.R. wrote the manuscript with input from all authors.

Competing interests

The authors declare no competing interests.

Additional information

Supplementary information The online version contains supplementary material available at https://doi.org/10.1038/s42005-022-00961-9.

Correspondence and requests for materials should be addressed to Sunghun Lee or Fabian Rotermund.

Peer review information *Communications Physics* thanks Turgut Yilmaz and the other, anonymous, reviewer(s) for their contribution to the peer review of this work.